Acta Materialia 282 (2025) 120454

Contents lists available at ScienceDirect

Acta Materialia

journal homepage: www.elsevier.com/locate/actamat

Full length article

Machine learning-augmented modeling on the formation of Si-dominated Non-β'' early-stage precipitates in Al-Si-Mg alloys with Si supersaturation induced by non-equilibrium solidification

Miao He [a], Yang Li [b], Bita Ghaffari [b], Yang Huo [b], Larry Godlewski [b], Mei Li [b,*], Yue Fan [a,*]

[a] Department of Mechanical Engineering, University of Michigan, Ann Arbor, MI 48109, USA
[b] Research and Advanced Engineering, Ford Motor Company, Dearborn, MI 48124, USA

ARTICLE INFO

Keywords:
Atomistic modeling
Machine learning
Defects evolution
Precipitates nucleation

ABSTRACT

Recent experiments have shown that Al-Si-Mg alloys solidified under high cooling rates may lead to the nucleation of Si-enriched clusters that are remarkably different from the conventional Mg-Si co-clusters (*e.g.* β'' particles), and yet the responsible mechanism remains to be elucidated. Here we tackle the problem using a multiscale modeling framework that integrates atomistic modeling, energy landscape sampling, and lattice-based kinetic Monte Carlo (kMC) simulation. The migration energy barriers for vacancy-mediated diffusion amid complex local chemical environments are predicted on-the-fly using a surrogate machine learning model. We discover that the actual vacancy-Si migration barriers are much lower than those assumed in the classic linear interpolation approximation. Such a strong deviation from conventional wisdom, in conjunction with differing Si solute composition, can lead to a great variety in the nucleated early-stage precipitates. More specifically, a high-level supersaturation of Si solute (*i.e.* $x_{Si}/(x_{Si}+x_{Mg}) > 0.75$) would lead to an unexpectedly high enrichment of Si in the nucleated clusters with the Si:Mg ratio up to 5~6; while at a lower-level supply of Si solute the Mg-Si co-clusters (*i.e.* Si:Mg ratio around 1~2) are nucleated instead. These findings provide a viable explanation for the diverse types of early-stage precipitates observed in various experiments, from Si-enriched precipitates in high-pressure die cast Al alloys to β'' particles in conventional casting and/or heat-treated alloys. The implications of our findings are also discussed.

Introduction

Al-Si alloys exhibit an excellent combination of properties, such as good castability, corrosion resistance, and high strength-to-weight ratio [1–5]. As a result, these alloys are widely employed as structural materials in aerospace and automobile industries [6–8]. To tune the Al-Si alloys' microstructures and subsequently their properties, additional minor elements have been introduced into the system [9–12], and an important species in (3xx- and 6xxx-series) alloys is Mg [13–17]. Energetic calculations in atomistic simulations [18,19] show that Mg can strongly bond with Si to form stable co-clusters in primary Al. Indeed, β phase precipitates, *e.g.*, Mg_2Si and Mg_5Si_6 have been widely reported in as-cast and heat-treated Al-Si-Mg alloys in experiments [20–23]. However, recent studies show that those β'' or β particles are absent in the Al-Si-Mg alloys solidified at high cooling rate. Instead, a significant amount of Si-enriched precipitates in primary Al have been observed in the alloys fabricated with high-pressure die casting (HPDC) and selective laser melting (SLM) [24–26], implying the early-stage nucleated clusters are also rich in Si. Indeed, high-resolution Atom Probe Tomography (APT) measurements show that the Mg:Si ratio in the precursor of those Si precipitates is around 1:4.5 [24], which is much lower than that observed in the β particles. Since the components produced using HPDC and SLM in industrial applications are often not solution heat treated, the misprediction on the nucleation of precipitates could inhibit our understanding of how the alloys would respond to the subsequent thermal exposures and their corresponding mechanical properties.

While there are speculations [26] that the absence of β particles may be related to the solidification rate and heat treatment, a mechanistic understanding is still missing. Intuitively, the manufacturing processes with extremely fast cooling rate can result in a higher level of supersaturated Si solutes in Al. However, whether the excess amount of Si

* Corresponding author.
E-mail addresses: mli9@ford.com (M. Li), fanyue@umich.edu (Y. Fan).

https://doi.org/10.1016/j.actamat.2024.120454
Received 5 July 2024; Received in revised form 17 September 2024; Accepted 4 October 2024
Available online 6 October 2024
1359-6454/© 2024 Acta Materialia Inc. Published by Elsevier Ltd. All rights are reserved, including those for text and data mining, AI training, and similar technologies.

solutes would lead to pronounced Si-rich precipitates is not self-evident. From the kinetics perspective, the migration barriers of Si and Mg in primary Al do not differ significantly in the classical linear interpolation approximation (LIA) model [27], implying the microstructural evolution of precipitates should be dominated by the thermodynamics driving force. Correspondingly, the LIA-based kinetic Monte Carlo (kMC) simulations show that the early-stage precipitates exhibit comparable fractions of Mg and Si [27]. Therefore, the formation mechanism of the heavily Si-enriched early-stage precipitates, as well as their sensitivity to the initial composition in primary Al, remain elusive.

In the present study, we develop an integrated computational framework that combines atomistic modeling, energy landscape sampling and lattice-based on-the-fly kMC simulation to investigate the vacancy diffusion-mediated microstructural evolution and precipitate nucleation in an Al-Si-Mg model system. The vacancy migration barriers needed in kMC are calculated using both the classical LIA model and the realistic nudged elastic band (NEB) algorithm, and a comparative analysis is thus made. Machine learning (ML) based surrogate models using multi-layer perceptron are also employed to accelerate the exploration of the vast phase space encompassing the vacancy's complex local chemical environments along with its diffusion and precipitate development. We discover that, compared with the classical LIA model, the realistic vacancy migration barriers calculated by NEB span a much broader range, and in particular the vacancy-Si migration barriers are significantly lower than the vacancy-Mg or vacancy-Al migration barriers. We further show that the strong deviation from the simple and perfect correlation between kinetics (*e.g.* migration barrier) and thermodynamics (*e.g.* configurations energy difference) assumed in LIA, in conjunction with an initial high-level supersaturation of Si solutes, make the early-stage precipitate clusters significantly different from β particles. In our findings, the early-stage clusters are Si-enriched with the Si:Mg ratio up to 5~6, consistent with the recent experiments mentioned above. Our simulations also demonstrate that, if the initial supersaturation level of Si solutes is less extreme then Mg-Si co-clusters would form, a phenomenon observed in traditionally cast or heat-treated Al-Si-Mg alloys. The sensitivity of Si content in the early-stage precipitate clusters to the solutes' concentration is also investigated. This integrated computational framework provides a physics-based predictive tool for the microstructural evolution in Al alloys processed under high cooling rates, which may lead to enhanced efficiency in alloy design for state-of-art structural castings in various industry sectors.

Materials and methods

Atomistic model setup and lattice-based on-the-fly kMC simulation

The scope of the present study focuses on vacancy diffusion-mediated microstructural evolution, so the key parameters ensuring a reliable modeling prediction are the vacancy migration barriers in the presence of various local chemical environments. Here we consider an Al-Si-Mg alloy model using a recently developed neural network interatomic potential [27] that has been more comprehensively calibrated with first-principle calculations compared with conventional potential developed using the embedded-atom method. A vacancy is created in a simulation box of $8 \times 8 \times 8$ face-centered cubic (FCC) unit cells with a periodic boundary condition, and the remaining lattice sites are randomly assigned to one of the three element types (*i.e.* Al, Si, Mg) based on the prescribed composition. Each of these atomic configurations is then allowed to evolve by conjugate gradient energy minimizations using the Large-scale Atomic/Molecular Massively Parallel Simulator (LAMMPS) software. In the present study, we assume the vacancy can only exchange with one of its 12 nearest neighbors.

As discussed in Sec. 1, two different methods are utilized to calculate the vacancy migration barriers. The first method is the widely adopted LIA model [27–29], in which the vacancy migration barrier, ΔE^m, is defined as:

$$\Delta E^m = \Delta E^m(Al) + \left(E_{final} - E_{init}\right)/2 \tag{1}$$

where E_{init} and E_{final} are the system's initial and final configurational energies, corresponding to before and after the vacancy migration, respectively. $\Delta E^m(Al)$ represents the vacancy migration barrier in a reference pure-Al matrix.

The other method employed is NEB [30], a potential energy landscape sampling algorithm that directly probes the minimum energy paths and hence identifies the migration barriers between the prescribed initial and final states. In this study, we use the NEB algorithm implemented in LAMMPS with 15 replicas and a force convergence criterion of 1×10^{-6}. Note that the LIA model essentially assumes a perfect and linear correlation between the kinetic diffusion barrier and thermodynamic energetics, while no such assumption is made in the NEB method and the migration barriers calculated by NEB are thus more reliable and physics-based.

In terms of computational costs, since the LIA model only needs the energetics calculations for the initial and final states instead of mapping the potential energy landscape, it is much faster than NEB. That said, to calculate the on-the-fly energetics and/or migration barriers at each vacancy hopping for millions of overall migration steps is still formidable, regardless of whether the LIA or NEB model is used. Therefore, two ML surrogate models are trained respectively based on the atomistic simulation results of the LIA and NEB methods, and these surrogate models are then adopted to efficiently obtain the needed migration energy barriers in kMC simulations. The detailed ML algorithms can be found below in Sec. 2.2.

The obtained chemical environment-sensitive migration barriers are then fed into a standard 1st-order kMC model to predict the vacancy-mediated microstructural evolution and early-stage precipitate nucleation. For each kMC step, the vacancy moves to one of its 12 nearest neighboring sites following the designated probabilities of:

$$P_i = \frac{R_i}{\sum_{k=1}^{12} R_k},\ i = 1, 2, \cdots 12 \tag{2}$$

where P_i is the probability of vacancy moving to its i^{th} nearest neighboring site during a given time step in kMC simulation. The corresponding migrating rate of this move, R_i, is given by

$$R_i = \Gamma_0 \exp\left(-\frac{\Delta E_i^m}{k_B T}\right) \tag{3}$$

where Γ_0 is the attempt frequency chosen here from earlier first-principle calculations in the order of Debye frequency $\sim 10^{13}\ s^{-1}$ [31], k_B is the Boltzmann constant, T is the temperature, and ΔE_i^m is the migration barrier for the vacancy to jump to the i^{th} nearest neighboring site. The time for each kMC step is calculated as

$$\Delta t = \frac{-\ln(r)}{\sum_{k=1}^{12} R_k} \tag{4}$$

where r is a random variable uniformly distributed within (0, 1].

It is worth noting that the simple implementation of such a 1st-order kMC algorithm in multi-component alloys may sometimes lead to trapping situations [32], and to address the problem a 2nd-order residence time algorithm [33–35] and kMC implementation are employed in the present study when needed. Further details of the hopping algorithms in kMC are included in the Appendix.

ML prediction of vacancy migration barriers

Typical kMC models may need millions of steps to capture the clustering phenomenon in a dilute alloy model [27,36–39]. Therefore, even though LIA is faster than NEB as discussed in Sec. 2.1, it is still computationally insurmountable to calculate the configurational

energies at each single step over the entire kMC simulation. In other words, regardless of LIA or NEB, it is imperative to develop and employ ML surrogate models that do not rely on actual interatomic force-field calculations to obtain the configurational energies and migration barriers to ensure computationally effective simulation.

The training dataset consists of ~40k atomistic simulations with different compositions and configurations. The scope of the present study focuses on typical cast Al-Si alloys with 7~10 % Si and <1 % Mg, *e.g.* AlSi7MgMn which has been widely used in large HPDC structural components in the automotive industry. Therefore, the compositional space concerned here is more extended in Si axis than in Mg axis. Considering the local chemical environment (*e.g.* near a vacancy) could be more extreme than the global composition of an entire sample, we thus probe a broader compositional space as marked in Fig 1.a. More specifically, as indicated by the blue squares in the left panel of the figure, the applicable compositional space is sampled uniformly. Based on each of these unique compositions, 1000 atomistic samples with random configurations are created, for which the configurational energies and vacancy migration barriers are calculated in LAMMPS. As illustrated in the right panel of Fig 1.a, we build an architecture of multi-layer perceptron, namely an artificial neural network (ANN) consisting of three hidden layers, where the number of hidden units in each consecutive hidden layer is $L_1 = 32$, $L_2 = 16$, and $L_3 = 8$, and the Rectified Linear Unit (ReLU) activation function is applied on each hidden layer. The input layer and output layer are adjusted accordingly to the key information needed in LIA or NEB. In particular, the input is a vectorized encoding sequence representing the sample's configuration (LIA model) or local chemical environment surrounding the vacancy-migrating atom pair (NEB model), and the output layer is represented by a single value of the sample's configuration energy (LIA model) or vacancy migration barrier (NEB model).

For example, LIA concerns the sample's energy at a given atomic configuration, and thus the input was chosen to be a vectorized representation of the sample's configuration while the output is the sample's configuration energy. Here we use a bond-counting model, which essentially encodes the various types of bonds in a given sample (*e.g.* vacancy-Al, vacancy-Mg, vacancy-Si, Al-Al, Mg-Mg, Si-Si, Al-Mg, Al-Si, Mg-Si) and their numbers into a 63 × 1 column vector as the training input (see Appendix for more details).

As for the training of surrogate model for NEB method, since the target is the migration barrier for a local vacancy hopping along a specific direction, caution has to be exercised when encoding the input vector. For example, assuming a vacancy migration direction of [0 −1/2 −1/2], as illustrated in Fig 1.b, the local chemical environment surrounding the vacancy-migrating atom pair is then ranked into a sequence based on their relative positions. More specifically, as shown in Fig 1.b, the migrating atom is labeled as position 0, while the four atoms closest to the vacancy and migrating atom are ranked 1–4, and the two atoms labeled as '5' and '6' are the nearest neighbors of the vacancy but the second nearest neighbor of the migrating atom. We label a total number of 101 atoms until the 5th nearest neighboring shell of the vacancy-migrating atom pair, in effect neglecting the influence of the atoms beyond the 5th shell on the vacancy's migration barrier. The sequence of those atoms is thus encoded into a 101 × 1 column vector, serving as the training input. If the vacancy is migrating along a different direction, then the surrounding 101 atoms need to be re-labeled through a coordination transformation to ensure a consistent encoding sequence. More details are provided in the Appendix. The atomistic samples and the ground-truth results are divided into 11 groups, in which the last group is used as the test datasets for evaluating the goodness of ML prediction shown below in Sec. 2.3, while the other groups of data are used for training the ML model through a 10-fold cross-validation

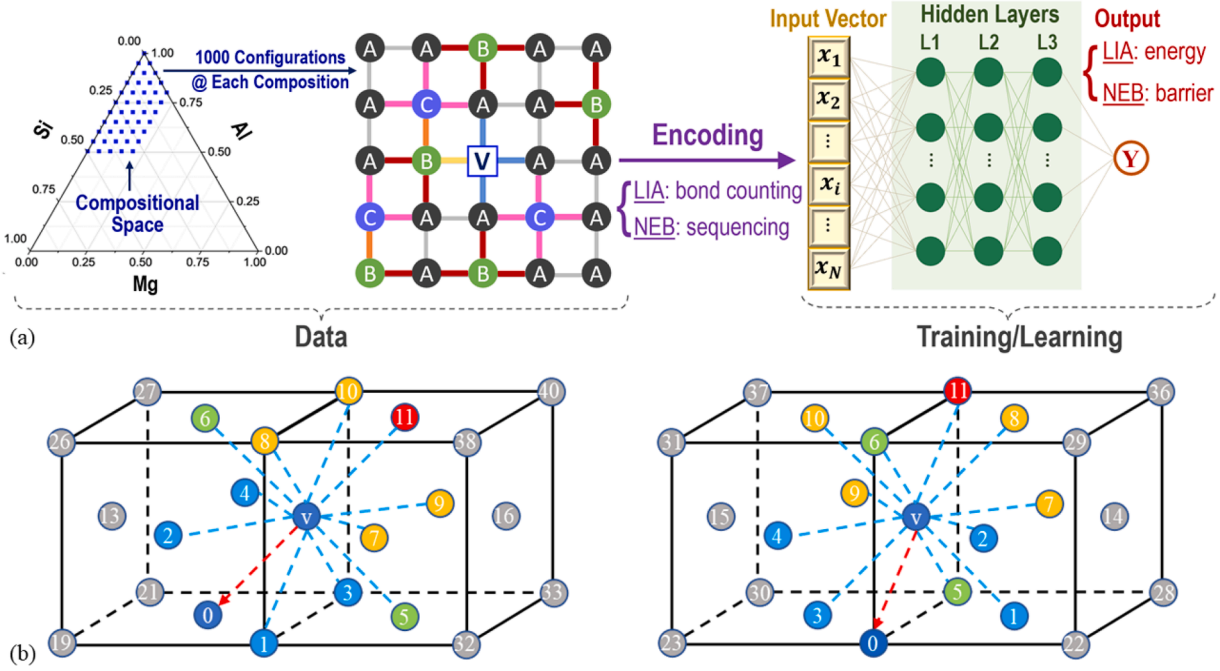

Fig. 1. (a) Schematic illustration of the computational framework that trains a surrogate ML model (right panel) based on LIA and NEB results (left penal). The left panel shows the phase space encompassing the chemical compositions of atomistic samples. The right panel shows the architecture of the artificial neural network for predicting the configurational energies and vacancy migration barriers. Three hidden layers are used to establish the non-linear relationships between the input vector and output. (b) Schematic illustration of how the local chemical environment surrounding the vacancy-migrating atom pair is encoded. Note that in the simulations, the local environment up to the 5th nearest neighboring shells is encoded, while here in this illustrative schematic only partial environments are displayed to avoid the plot from being too crowded. The letter v denotes the vacancy, the numbers in the left panel denote the position of the atom in the encoding sequence, and the arrows show the vacancy migration direction. The color of atoms representing the encoding is based on their distance to the vacancy-migrating atom pair. The left and right panels correspond to encoding with different vacancy migration directions of [0 −1/2 −1/2] and [1/2 0 −1/2], respectively.

method. It is worth noting that the reason of selecting 5 nearest shells here is twofold: First, earlier literatures show that 3~7 nearest shells are sufficient to provide reliable predictions on the vacancy migration barriers in multi-components alloys [37,38]; Second, from the perspective of computational efficiency, including atoms beyond the 5th neighboring shell into the encoding sequence would considerably increase the number of parameters and training efforts. Moreover, higher number of parameters may lead to the risk of overfitting, which could compromise the accuracy and robustness of the machine learning model, thus requiring much larger training dataset. Therefore, considering that 5 nearest shells already entail quality information with acceptable errors (see Sec. 2.3 for further discussions), we hence adopt such a cut-off to strike a balance between the computational accuracy and efficiency.

Self-Consistency alignment on the ML-Predicted vacancy migration barriers

Fig 2a shows the performance of the ML model for the sample configuration energies (to be used mainly in LIA-based kMC) and the vacancy migration barriers (to be used in NEB-based kMC). Both predictions are in good agreement with the ground-truth results directly calculated by LAMMPS. Within the same ML architecture, the energy prediction yields higher accuracy (*i.e.* larger R^2 value) than the migration barrier prediction does. Before passing these surrogate model-predicted results to kMC simulations, a self-consistency alignment has to be implemented to make certain the inevitable ML-prediction errors do not compromise the real physics. More specifically, as illustrated in Fig 2b, in a real physical two-state hopping process in the energy landscape, the states' configurational energetics and their connecting migration barriers have to strictly follow the condition:

$$\Delta E^m_{A\to B} - \Delta E^m_{B\to A} \equiv E_{conf,A} - E_{conf,B} \tag{5}$$

where $\Delta E^m_{A\to B}$ and $\Delta E^m_{B\to A}$ are the migration barriers associated with the forward and backward jumps between A and B states, while $E_{conf,A}$ and $E_{conf,B}$ are the system configurational energies at A and B states, respectively.

In the surrogate model trained based on LIA, the migration barriers are not directly calculated but instead interpolated on the configurational energies of states A and B. Therefore, the self-consistency requirement mentioned above is naturally satisfied. In other words, as long as a given configuration can be encoded into a unique input vector, no additional alignments regarding the kinetics-thermodynamics consistency need to be implemented. It is worth noting, though, such a numerical self-consistency does not necessarily lead to more reliable results, as aforementioned in Sec. 2.1.

On the other hand, in the surrogate model trained based on NEB calculations, the self-consistency requires extra caution. In particular, inconsistency may occur if the prediction error for $\Delta E^m_{A\to B}$ cannot be completely canceled by the prediction error for $\Delta E^m_{B\to A}$. To address such an issue and enforce the consistency, we make the following correction/alignment:

$$\Delta E^m_{A\to B,c} \equiv \Delta E^m_{A\to B} + \frac{\Delta E^m_{B\to A} - \Delta E^m_{A\to B} + E_{conf,B} - E_{conf,A}}{2} \tag{6}$$

With such alignment, it is guaranteed that $\Delta E^m_{A\to B,c} - \Delta E^m_{B\to A,c} \equiv E_{conf,B} - E_{conf,A}$. The so-aligned $\Delta E^m_{A\to B,c}$ is thus fed into the NEB-based kMC simulation in the present study. Note that compared with the 1st term on the right hand side of Eq. (6), the alignment term is much smaller (more details in Appendix 4).

Before presenting the main results in Sec. 3, it is worth discussing a few remarks on the ML training and alignment introduced above. Admittedly, there is room for further optimization on the training/predicting results, *e.g.* by increasing the volume of the training dataset, by encoding larger shell information into the present ML model, or even by employing alternative ML architectures [40–41,42]. That said, the main objective of the present study is not to pursue the highest numerical precision, but to reveal the underlying physics of the formation of non-β'' early-stage precipitates within an acceptable numerical error range. In this regard, the 0.04 eV MAE of the predicted vacancy migration barriers is comparable to the ~35 meV-level MAE in other multi-component alloys studies [38] and hence acceptable.

Results and discussions

Sensitivity of vacancy migration barriers to chemical environments and fast Si diffusion

The vacancy migration barriers calculated based on LIA and NEB methods from the training dataset are compared in Fig 3. The three plots in Fig 3.a show the distributions of activation barriers for different migrating atoms. First, it can be seen that the LIA results do not show a strong dependence on chemistry, and all three distributions exhibit relatively narrow and symmetric profiles with respect to

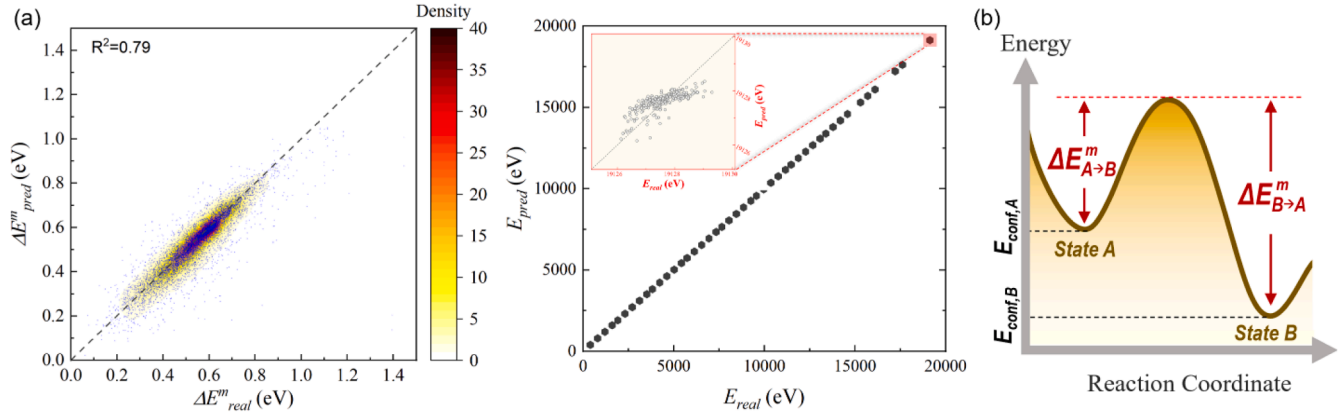

Fig. 2. (a) Scatter plots illustrating the comparison between ML predictions and real values for vacancy migration barriers ΔE^m (left panel) and configurational energies E (right panel). The inset in the middle panel shows a zoomed view of the comparison between predicted and real configurational energies within a narrow range marked by the red square. The MAE and RMSE for the training on vacancy migration barriers are 0.04 eV and 0.06 eV, respectively. While for the training of the system's configurational energy, the MAE and RMSE are 0.37 meV/atom and 0.56 meV/atom, respectively. Note that while the R^2 of the model is not ideal (0.79), considering the physics complexity of such a problem, the quality of the ML surrogate model is reasonably good. (b) Schematic illustration of a two-state hopping between state A and state B in the energy landscape.

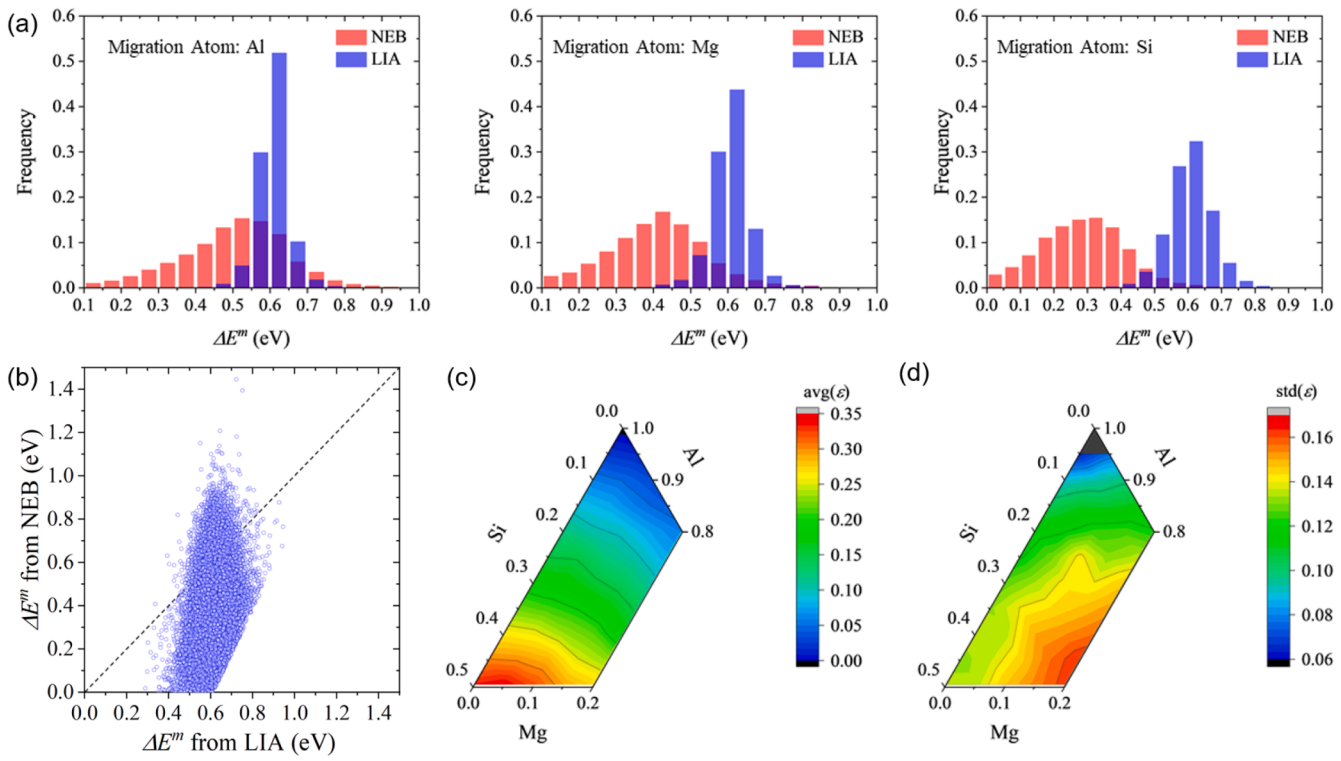

Fig. 3. (a) Distribution of vacancy migration barriers towards different migrating atoms calculated from NEB (red) and LIA (blue) methods; (b) One-on-one correspondence between NEB and LIA results; (c) Distribution of average, and (d) standard deviation of the difference between LIA and NEB results in the ternary phase diagram.

$\Delta E^m(Al) = 0.61\ eV$ (*i.e.* the vacancy migration barrier in a reference pure-Al matrix). Note that given the definition of the LIA model discussed above in Sec. 2.1, this result is as expected. On the other hand, the NEB results are remarkably different and much more broadly distributed, including some very low-barrier migrations. The NEB results also reflect strong chemical sensitivity, and in particular, the migration barriers for the vacancy to nearby Si sites are considerably lower (in a statistical sense, see Appendix 5 for more details) than those to nearby Al or Mg sites. Fig 3.b shows the correlation between the ΔE^m computed using NEB and LIA methods for the same hopping process. For the vast majority of atomic configurations in the data set, the migration energy barriers from NEB calculations are smaller than those computed using LIA method.

To better understand the deviations between the LIA and NEB results (defined as $\varepsilon = \Delta E^m_{LIA} - \Delta E^m_{NEB}$), as well as their variations in the chemical space, in Fig 3.c and 3.d we plot the average value and standard deviation of ε, respectively, in the ternary phase diagram. For the *avg(ε)* plot, it can be seen that the LIA-NEB differences disappear in the dilute limit (*i.e.* almost pure Al environment) but gradually increase in more Si-enriched environment, indicating Si diffusion should be systematically faster in NEB-based kMC than in LIA-based kMC. In other words, this suggests that the conventional LIA-based kMC modeling may lead to mispredictions of the formation of early-stage clusters, specifically in the range of initial Si composition of the interest of this study. As for the *std(ε)* plot, the results again vanish in the dilute limit. However, the largest standard deviation does not occur in the Si-enriched region but instead is present in the Mg-enriched region, indicating a more complex role of Mg in vacancy-mediated diffusion. While the initial condition with significant Mg supersaturation in primary Al is not within the scope of the present study, this observation might be worthy of further investigation when the material of interest is Al-Mg casting alloy families.

Formation of Si-rich clusters in the early-stage precipitation in NEB-based kMC

With the vacancy migration barriers obtained from the ML models in Sec. 3.1, a series of kMC simulations is then conducted, as discussed in this and the following sections, to systematically investigate the nucleation of early-stage precipitates under different model assumptions and various initial conditions. It was found that NEB-based kMC in general yields more Si-enriched clusters than LIA-based kMC does, and quantitative differences between the two models are sensitive to the initial content of Si solute in the system. As a representative example, Fig 4.a shows the significant differences in the energy evolution curves predicted by the two models at 300 K and over 20 million kMC steps from an identical initial random solid solution state at 5 at% Si and 0.5 at% Mg. More specifically, in LIA-based kMC, the energy of the system manifests a steady descending trend from the very early stage, indicating that a low-barrier hopping is very likely to lead to an energy reduction. Such a strong kinetics-thermodynamics coordination is not surprising because, as discussed above in Sec. 2.1, the kinetic diffusion barrier in the LIA model adopts a perfect and linear correlation with the thermodynamic energetics. In contrast, the energy evolution curve in NEB-based kMC almost remains flat in the early stage and does not start to descend until after 10^5 kMC steps. This suggests that the fast diffusion paths of vacancy in Al-Si-Mg alloys, at least in the solid solution states, do not necessarily align with the thermodynamic driving force in a simple manner as assumed in the classical picture. As discussed below, this could have significant implications for the development of early-stage precipitates in alloys subjected to far-from-equilibrium processing conditions.

In addition to the energy evolution curves, the microstructures of the early-stage precipitates predicted by the two models are also distinct from each other. As seen in Fig 4.b, the cluster nucleated in LIA-based kMC simulation contains Si and Mg with a ratio ~1.5; while in NEB-

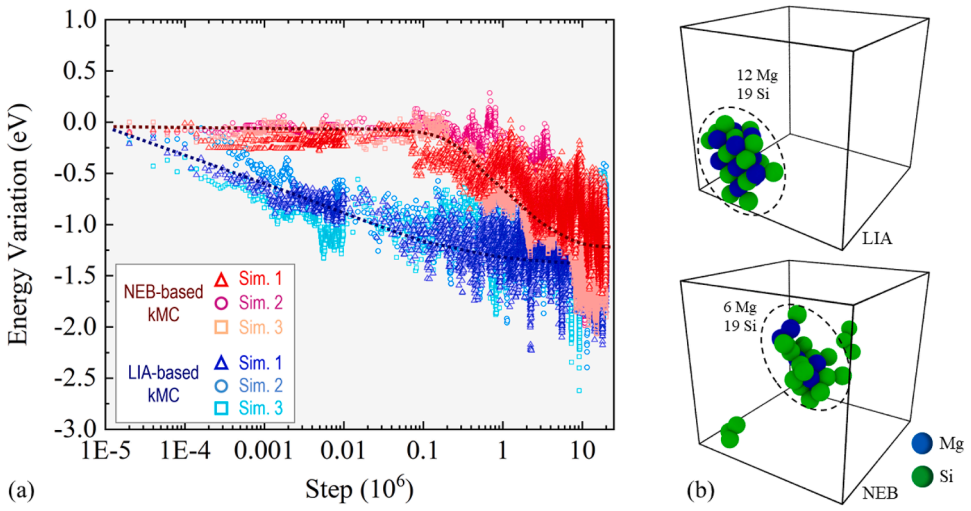

Fig. 4. (a) Evolutions of system energy *versus* step for NEB- and LIA-based kMC simulations. Each simulation is performed 3 times from independent initial atomic configurations with fixed composition (5 at% Si and 0.5 at% Mg). (b) Representative atomic configurations of the solute clusters after the LIA- and NEB-based kMC simulations. Individual solute atoms and clusters containing 2 atoms are not shown.

based kMC, the nucleated cluster is considerably Si-enriched with a Si:Mg ratio larger than 3. This is because the LIA-based kMC is essentially driven by thermodynamics only, and with the low energetics nature of Mg-Si co-clusters [18,19], the early-stage precipitates include a comparable amount of Si and Mg even though more Si atoms than Mg atoms (5 at% *vs.* 0.5 at%) present in the initial random solid solution state. On the other hand, the vacancy-mediated Si diffusion is much faster than other species in NEB-based kMC (Fig 3.a). Hence, with the initial high-level supersaturation, Si solutes very likely agglomerate first without much reduction in the energetics. Then, the fast-moving small Si clusters become significantly stabilized when they meet Mg solutes in the matrix. This explains why in NEB-based kMC the energy evolution profile is almost flat in the beginning and drops later, and why the nucleated precipitates are decorated with only a minor amount of Mg.

To further illustrate how LIA- and NEB-based kMC simulations lead to significantly different compositions in the nucleated clusters, we trace the time evolution of vacancy's local chemical environments (*i.e.* within 5th nearest neighboring shell) in the ternary phase diagram. As exemplified in Fig 5, both simulations start from the same initial configuration, and yet the evolution trajectories are remarkably different from each other. In the LIA-based kMC, there is no clear trend/direction of the evolution, except that Al content near the vacancy decreases, indicating the forming of Mg-Si co-clusters. In contrast, there exhibits a strong and consistent trend towards a Si-rich region in the NEB-based kMC, and such a consistent enrichment of Si surrounding the vacancy explains the observed high Si:Mg ratio in Fig 4.b.

Effect of initial Si supply on the Si:Mg ratio in the early-stage precipitate clusters

We further investigate the effect of initial composition by conducting a series of kMC simulations at various Mg and Si concentra-

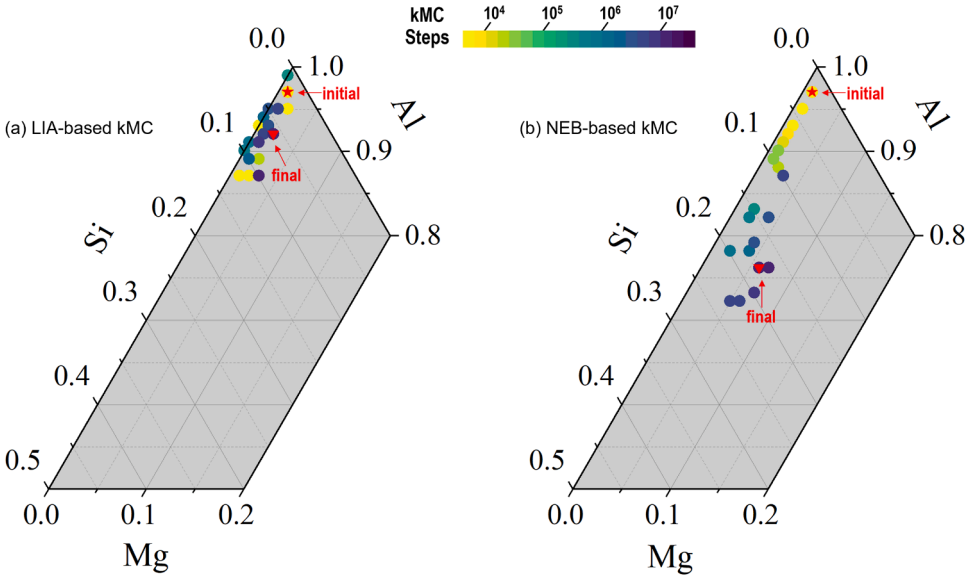

Fig. 5. Evolution of the local chemical composition within the 5th nearest neighboring shell surrounding the vacancy during kMC simulations. (a) and (b) are results predicted from LIA- and NEB-based kMC simulations, respectively, for the same starting atomic configuration. The points are colored based on the log of the kMC step. The initial and final chemical compositions surrounding the vacancy are remarked by red star and triangle, respectively.

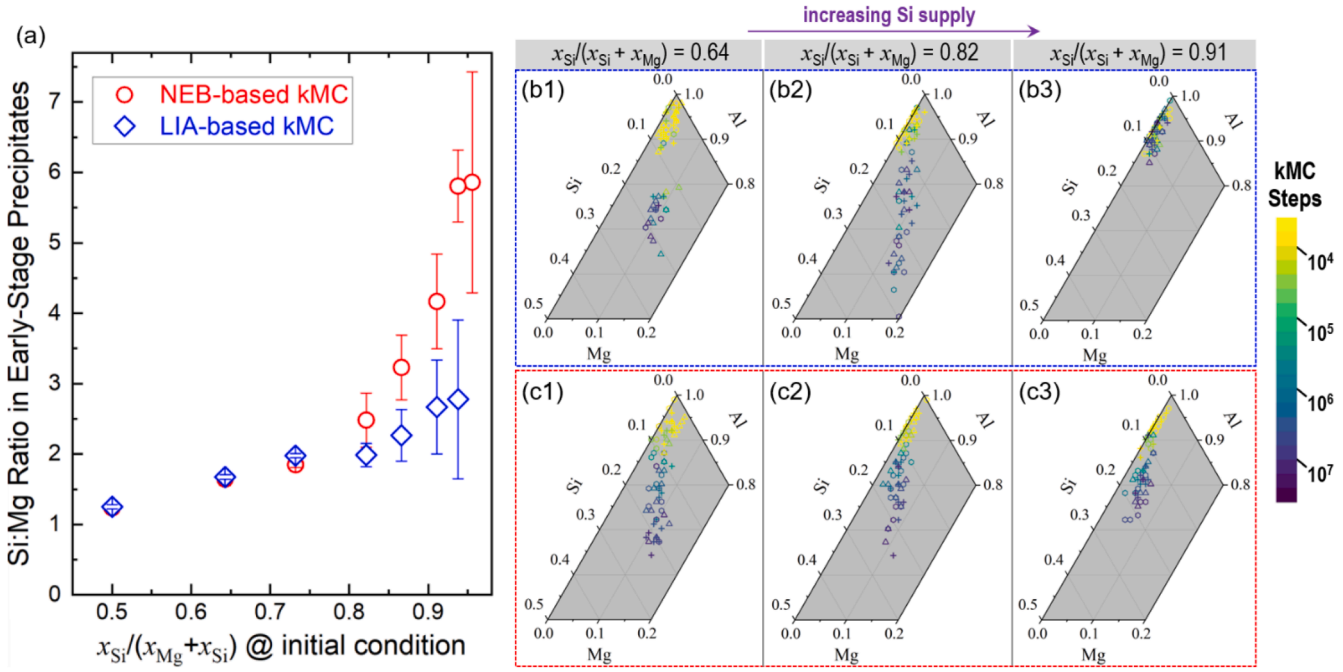

Fig. 6. (a) Predictions of the Si:Mg ratio in early-stage precipitates by kMC simulations as a function of initial Si solute content, indicated by $x_{Si}/(x_{Si}+x_{Mg})$. The data points are calculated as the average ratio from 3 independent kMC simulations, and the error bars represent the standard deviation of the mean values. Red circles correspond to NEB-based kMC simulations, and blue diamonds correspond to LIA-based kMC simulations. (b, c) Evolution of the local chemical composition within the 5th nearest neighboring shell surrounding the vacancy during the (b) LIA-based and (c) NEB-based kMC simulations. The initial values of $x_{Si}/(x_{Si}+x_{Mg})$ are shown above the panels. Three independent random configurations are generated for each initial composition, and the results for each simulation are plotted by hexagons, triangles, or crosses, and colored based on the log of the kMC step.

tions while keeping the Al content fixed (94.5 at%). For each initial composition, three independent simulations are performed with random atomic configurations. Fig 6.a shows the dependence of Si:Mg ratio in the early-stage precipitate clusters on the levels of initial Si solute supply. It can be seen that, as long as the initial Si solute concentration is not extremely high (*i.e.* $x_{Si}/(x_{Si}+x_{Mg}) < 0.75$), LIA- and NEB-based kMC results do overlap. Both models yield comparable amounts of Si and Mg in the nucleated clusters with the Si:Mg ratio between 1 and 2, which are in line with the conventionally observed Guinier-Preston zones or β'' clusters. However, by further increasing the relative initial concentration of Si solute, the two models predict remarkably different results. More specifically, the LIA-based kMC only exhibits a very mild increase of Si content in the nucleated clusters; while the NEB-based kMC shows a much more pronounced enrichment of Si, due to the preferential vacancy-mediated Si diffusion discussed above. In particular, the clusters' Si:Mg ratio predicted by the NEB-based kMC can go beyond 5, which is consistent with the recent HPDC experiments [24].

We show in Fig 6.b-c a few representative trajectories of the vacancy's local chemical environment evolution at different initial $x_{Si}/(x_{Si}+x_{Mg})$, namely (i) 0.64, (ii) 0.82, and (iii) 0.91. For scenario (i) where the initial Si level is not extremely high, both LIA- and NEB-based kMC give analogous ending positions in the ternary phase diagram (seen in Fig 6. b1 and c1), indicating similar Si:Mg participation ratio in the development of early-stage precipitates. For scenario (ii), the ending position in Fig 6.b2 is generally more Mg-rich than that in Fig 6.c2, indicating again that the LIA-based kMC is essentially driven by thermodynamics alone. For scenario (iii) with an even higher level of initial Si solute supply, the contrasts of the ending positions in these two models become more obvious, with a much higher level of Si enrichment in the NEB-based kMC results. To summarize, these results demonstrate that, due to its inability to describe the accurate vacancy-diffusion kinetics, the LIA-based kMC cannot capture the significantly Si-enriched precipitates observed in recent experiments. In other words, the nucleation of significantly Si-enriched precipitates relies on two stringent conditions: first, there needs to be a very high level of supersaturated Si solutes in the primary Al from the beginning; second, the vacancy-mediated diffusion of Si must be much faster than the diffusion of other species in Al-Si-Mg alloys. This can explain why Si-enriched precipitates are only observed in the alloys with far-from-equilibrium processing histories without solution heat treatment [24–26], but not in conventional cast and/or heat-treated alloys, and why they have never been predicted by earlier LIA-based modeling studies [27].

Conclusions

This study investigates the nucleation of early-stage precipitates in Al-Si-Mg alloys with high levels of supersaturation of Si solute using ML-augmented kMC simulations. The main conclusions of the present study are summarized below:

- The conventional LIA model, which assumes a simple and perfect correlation between kinetics (*e.g.* vacancy migration barriers) and thermodynamics (*e.g.* configurational energetics differences before and after vacancy hopping), displays grave shortcomings in modeling early precipitation in Al-Si-Mg alloys. In particular, in contrast to LIA predictions, the migration energy barriers predicted using NEB method for vacancy-mediated diffusion of Si atoms are significantly smaller than the diffusion of Al or Mg atoms.
- The observed preferential migration of Si atoms, in conjunction with an initially high supply of supersaturated Si solutes (*i.e.* $x_{Si}/(x_{Si}+x_{Mg}) > 0.75$), could lead to a remarkable enrichment of Si in the early-stage precipitate clusters with the Si:Mg ratio up to 5~6, which significantly deviates from the compositions in conventional β'' or β particles.

- These findings not only provide a viable understanding of the recently observed Si-enriched precipitates in HPDC and SLM experiments, but also explain the formation of Mg-Si co-clusters in traditionally cast or heat-treated alloys. Therefore, our findings present an essential improvement to physics-based predictive capabilities that would ultimately allow synergistic utilization of alloy chemistry and processing conditions to fully understand and optimize the microstructural evolution in Al alloys.

CRediT authorship contribution statement

Miao He: Writing – review & editing, Writing – original draft, Visualization, Methodology, Investigation, Formal analysis, Data curation. **Yang Li:** Writing – review & editing, Resources, Project administration, Methodology, Investigation, Funding acquisition, Conceptualization. **Bita Ghaffari:** Writing – review & editing, Investigation, Formal analysis. **Yang Huo:** Writing – review & editing, Resources, Investigation. **Larry Godlewski:** Writing – review & editing, Resources, Investigation. **Mei Li:** Writing – review & editing, Visualization, Project administration, Investigation, Funding acquisition, Conceptualization. **Yue Fan:** Writing – review & editing, Writing – original draft, Supervision, Resources, Funding acquisition, Conceptualization.

Declaration of competing interest

The authors declare that they have no known competing financial interests or personal relationships that could have appeared to influence the work reported in this paper.

Acknowledgements

The authors gratefully acknowledge the financial support by the University Research Program from Ford Motor Company. The authors thank insightful discussions with Drs. Fei Xue and Fei Wang at Ford Motor Company. M.H. and Y.F. also thank Dr. Zhucong Xi and Prof. Liang Qi from the University of Michigan for the very helpful discussions. Y.F. would like to acknowledge that the multi-components alloy model set up and analyses are based upon work support by NSF under Grant No. DMR-1944879.

Appendix

1. 2nd-order algorithm for kMC simulations

In the conventional 1st-order kMC algorithm, each vacancy jump considers only its first nearest neighbor sites. The simplicity of such an algorithm may under some circumstances lead to two issues. The first issue is the so-called trapping situation, where the system continues visiting the same few states. We illustrate in Fig A1a one of the trapping scenarios observed in our present study using the 1st-order kMC algorithm. More specifically, there are 5 states (A, B, C, D and E) involved in this situation, and the associated inter-state migration probabilities are listed along with the migration paths. Once the system jumps from state A to state B due to stochastic hopping, it will keep circulating among states B through E. Residence probabilities at different states are also marked in the graph. Because the sum of probabilities from any one of these states to hop to the other three states is >99 %, it is almost impossible for the system to escape from the cluster of these states. As a result, it becomes very inefficient to capture the microstructural development. The second issue is that, once the trapping scenario occurs and the involved migration barriers are too low (with respect to temperature), then the advance of timeclock in the kMC would become ineffective.

Here we adopt a 2nd-order residence time algorithm [32–35] to address these issues. In contrast to the 1st-order algorithm, where each vacancy jump is only determined by the migration barriers towards its 12 nearest neighbors, the 2nd-order algorithm accounts for two-step vacancy jumps, from the previous state j to the current state k, and further to the next state i. The probabilities for the vacancy migrating to state i are modified as:

$$P_i^{(2)} = \begin{cases} \dfrac{\beta_{ki}^f}{1-P_{kj}} \dfrac{\gamma_{kj}^b}{\beta_k^f}, & i = j \\ \dfrac{\beta_{ki}^f}{1-P_{kj}} \left(1 + \dfrac{\gamma_{kj}^b}{\beta_k^f}\right), & i \neq j \end{cases} \tag{S1}$$

where P_{kj} is the probability for the vacancy migration from state k to state j, $\beta_{ki}^f = P_{ki}(1-P_{ik})$ corresponds to the probability that the vacancy does not jump back to the current state k, $\beta_{ki}^b = P_{ki}P_{ik}$ denotes the probability that the vacancy jumps from k to i and then jumps back to k, $\beta_k^f = \sum_i \beta_{ki}^f$ denotes the probability that the vacancy will not jump back, $\beta_k^b = \sum_i \beta_{ki}^b$ is the probability that a backward jump occurs, $\gamma_{kj}^f = \sum_{i\neq j} \beta_{ki}^f$ and $\gamma_{kj}^b = \sum_{i\neq j} \beta_{ki}^b$. It can be proved that $\sum_i P_i^{(2)} = \frac{\gamma_{kj}^f + \gamma_{kj}^b}{1-P_{kj}} = 1$. Following such second-order residence time algorithm, the time for each kMC step is then modified as

$$\Delta t^{(2)} = \frac{-\ln(r)}{1-P_{kj}} \left[\gamma_{kj}^f \Delta \bar{t}_k{}^{(1)} + \gamma_{kj}^b \left(\Delta \bar{t}_k{}^{(1)} + t_{sj} + \frac{\beta_k^b}{\beta_k^f} t_s\right)\right] \tag{S2}$$

$\Delta \bar{t}_k{}^{(1)} = \frac{1}{\sum_{i=1}^{12} R_i}$ is the average time for vacancy migration from current state k to next state i with the first-order algorithm, $t_{sj} = \frac{1}{\gamma_{kj}^b} \sum_{i\neq j} (\Delta \bar{t}_k{}^{(1)} + \Delta \bar{t}_i{}^{(1)}) \beta_{ki}^b$, and $t_s = \frac{1}{\beta_{kj}^b} \sum_i (\Delta \bar{t}_k{}^{(1)} + \Delta \bar{t}_i{}^{(1)}) \beta_{ki}^b$.

To compare the efficacy of timeclock advance in the 1st- and 2nd-order algorithms, we show the histograms of time advances (in unit of s) for every 1000 kMC steps. It can be seen that the 2nd-order algorithm exhibits a bell-shape distribution with the mean value around 0.1–1 μs; while the 1st-order algorithm yields a broader distribution with a long tail in the very small timescale, indicating a less effective timeclock advance. The inset plot in Fig A1b shows the timeclock evolution as a function of kMC steps, and it is clear that the 2nd-order algorithm is more effective in reaching to longer timescale compared with the conventional algorithm.

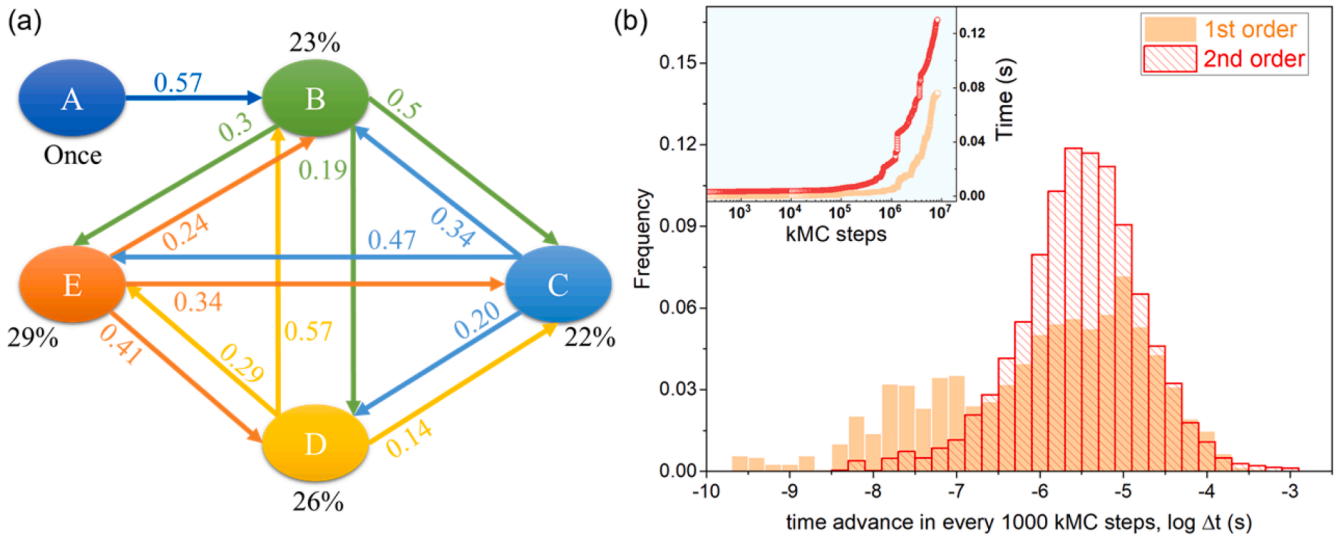

Fig. A1. (a) Illustration of a vacancy trapping situation observed in the 1st-order kMC simulation. The percentages of time the vacancy resides in various states are marked in black. The arrows with numbers show the direction and probability of the vacancy hopping, colored based on the starting state of the jumps. (b) Histograms of the timeclock advance for every 1000 kMC steps in the 1st- and 2nd-order algorithms. Inset plot shows the timeclock evolution as a function of kMC steps.

2. *Bond-counting method for predicting the sample configurational energy*

In this study, machine learning models based on the ANN architecture (Fig 1a) are built to predict the configurational energy and migration barrier based on the local chemical environment. To train the ML model for the system's configurational energy, a surrogate bond-counting method is used to encode the system atomic configuration as an input of the ANN. In particular, the number of different interatomic bonds is counted and vectorized to represent the atomic configuration. For each atom, we count the interatomic interactions within each nearest neighboring shell, up to the 7th neighboring shell. In the Al-Si-Mg system with a vacancy, 9 types of interacting pairs (vacancy-Al, vacancy-Mg, vacancy-Si, Al-Al, Mg-Mg, Si-Si, Al-Mg, Al-Si, Mg-Si) are considered. As a result, the atomic configuration can be represented by a vector with a length of $9 \times 7 = 63$, in which each element corresponds to the number of certain interatomic pairs in a certain neighboring shell.

3. *Encoding of local chemical environment and coordination transformation*

In the kMC simulations, the vacancy can jump to any of its 12 nearest neighbors, resulting in 12 possible migration directions. For the migration direction of [0 −1/2 −1/2] (benchmark), the migration barrier can be directly predicted from the ML model trained on NEB data, in which an encoding algorithm is implemented to convert the atom types surrounding the vacancy-migrating atom pair into a ranked input sequence, as seen in the left panel of Fig 1b. For a migration direction different from [0 −1/2 −1/2], the training input vector needs to be rearranged to ensure a consistent encoding sequence, in which the rank of each atom in the sequence is based on the same type of mapping from its relative position to the vacancy-migrating atom pair. For example, as shown in the right panel of Fig 1b, in which the migration direction is changed to [1/2 0 −1/2], the four atoms ranked 1–4 in the left panel of Fig 1b are no longer nearest neighbors of the vacancy and migrating atom. However, the system for [1/2 0 −1/2] migration direction can be regarded as a rotation of the benchmark system by 90° about the z-axis. Therefore, the new atomic coordinates relative to the vacancy in the encoding sequence can be transformed utilizing $x' = -y$, $y' = x$, and $z' = z$, where x, y, and z are the atomic coordinates relative to the vacancy in the benchmark system. Under such coordinate transformation, the atoms ranked 1–4 in the sequence are changed from the light blue atoms in the left panel to those in the right panel in Fig 1b. Table A1 shows the coordinate transformations for all 12 possible migration directions. By applying these transformations on the coordinates relative to the vacancy for all 101 atoms in the encoding sequence in the benchmark system, a new sequence of atomic coordinates relative to the vacancy can be obtained, resulting in a consistent representation of atomic configurations surrounding the vacancy-migrating atom pair but with a different migration direction.

Table A1
Coordinate transformations for different migration directions, corresponding to a rotational operation of the benchmark system (with the migration direction of [0 −1/2 −1/2]), from which a consistent atomic sequence representing the local chemical environment can be obtained compared to the benchmark system.

Migration Direction	Rotational Operation	x Coordinate Transformation	y Coordinate Transformation	z Coordinate Transformation
[0 −1/2 −1/2]				
[0 1/2 −1/2]	90° around x	x' = *x*	y' = -z	z' = *y*
[0 1/2 1/2]	180° around x	x' = *x*	y' = -y	z' = -z
[0 −1/2 1/2]	270° around x	x' = *x*	y' = *z*	z' = -y
[−1/2 0 −1/2]	270° around z	x' = *y*	y' = -x	z' = *z*
[1/2 0 −1/2]	90° around z	x' = -y	y' = *x*	z' = *z*
[1/2 0 1/2]	270° around x, 90° around z	x' = -z	y' = *x*	z' = -y
[−1/2 0 1/2]	270° around x, 270° around z	x' = *z*	y' = -x	z' = -y
[−1/2 −1/2 0]	90° around y	x' = *z*	y' = *y*	z' = -x
[−1/2 1/2 0]	270° around y, 180° around z	x' = *z*	y' = -y	z' = *x*
[1/2 −1/2 0]	270° around y	x' = -z	y' = *y*	z' = *x*
[1/2 1/2 0]	90° around y, 180° around z	x' = -z	y' = -y	z' = -x

4. Alignment term in Eq. (6)

In Fig A2 below, we show the correlation between the non-aligned migration barrier (the 1st term in Eq. (6)) and the alignment (the 2nd term in Eq. (6)) for all our ML training data, as well as their own distributions in the inset plot. It can be seen that, the alignment term is distributed very narrowly and symmetrically around 0 with the half-peak width ~0.05 eV, while the 1st term distributes broadly between 0 and 1 eV. In addition, according to the scattered plot there are no meaningful correlations between the two terms, meaning the alignment won't lead to statistical bias to the kinetics prediction of the kMC results.

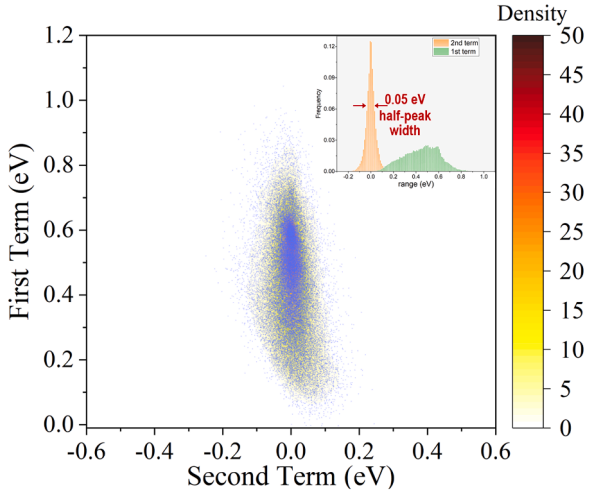

Fig. A2. The correlation between the alignment term (2nd term in Eq. (6)) and the non-aligned barrier (1st term in Eq. (6)), as well as their own distributions. It can be seen that the alignment term only gives a very small and non-biased minor correction to the 1st term, which does not largely impact the kMC results.

5. Compositional dependence of V-Si and V-Mg migration barriers

In the main text it has been shown that statistically the vacancy-Si migration barriers are lower than that for V-Mg migrations. That said, it is still possible that, at the same composition the V-Mg barrier could be lower than that of V-Si. At first, even at a fixed nominal composition of the entire sample, the atomic-level local environments are still diverse and, subsequently, lead to a distribution of migration barriers. More specifically, at the same nominal composition, we calculated the minimum barrier for Mg migration, $\Delta E^m_{Mg,\ min}$, the minimum barrier for Si migration, $\Delta E^m_{Si,\ min}$, the average barrier for Mg migration, $\Delta E^m_{Mg,\ avg}$, and the average barrier for Si migration, $\Delta E^m_{Si,\ avg}$. The differences of $\left(\Delta E^m_{Mg,\ min} - \Delta E^m_{Si,\ min}\right)$ and $\left(\Delta E^m_{Mg,\ avg} - \Delta E^m_{Si,\ avg}\right)$ across various nominal compositions are shown below in Fig A3. It can be seen that, in some compositional space (*e.g.* blue regions in the left panel), the minimum value of Mg migration barrier could be smaller than that of the minimum Si migration barrier, although statistically the average Si migration barriers are always lower than the average Mg migration barriers (seen in the right panel).

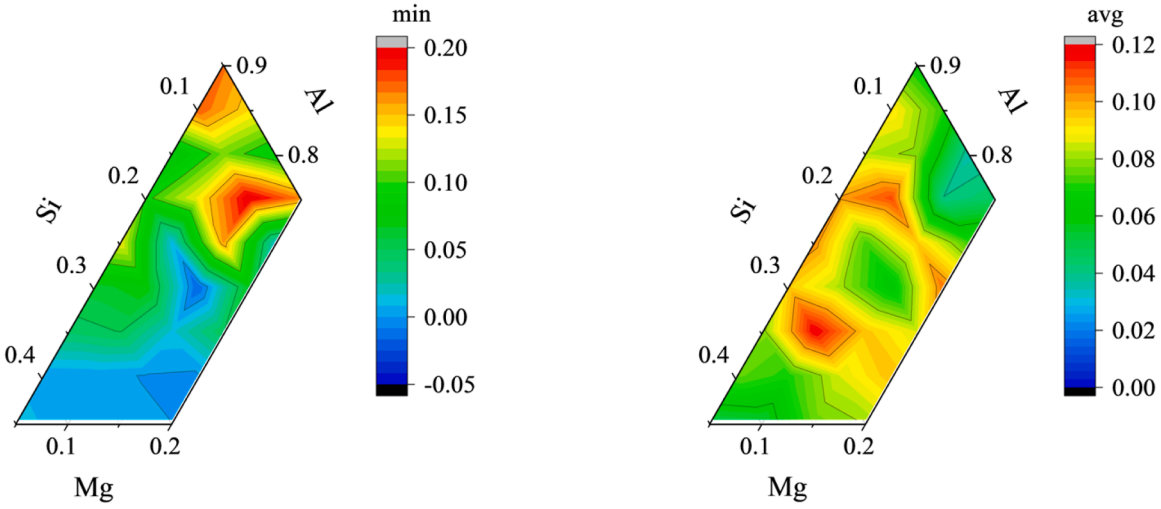

Fig. A3. The differences of $\Delta E^m_{Mg,\ min} - \Delta E^m_{Si,\ min}$ (left) and $\Delta E^m_{Mg,\ avg} - \Delta E^m_{Si,\ avg}$ (right) across various nominal compositions.

References

[1] V.C. Srivastava, R.K. Mandal, S.N. Ojha, Microstructure and mechanical properties of Al-Si alloys produced by spray forming process, Mater. Sci. Eng. 304-306 (2001) 555–558.

[2] S.G. Shabestari, H. Moemeni, Effect of copper and solidification conditions on the microstructure and mechanical properties of Al-Si-Mg alloys, J. Mater. Process. Techn. 153-154 (2004) 193–198.

[3] K.T. Chiang, N.M. Liu, T.C. Tsai, Modeling and analysis of the effects of processing parameters on the performance characteristics in the high pressure die casting process of Al-Si alloys, TInternat. J. Adv. Manufact. Techn. 41 (2009) 1076–1084.

[4] Y. Birol, Impact of grain size on mechanical properties of AlSi7Mg0.3 alloy, Mater. Sci. Eng. 559 (2013) 394–400.

[5] X. Jiao, C. Liu, J. Wang, Z. Guo, J. Wang, Z. Wang, J. Gao, S. Xiong, On the characterization of microstructure and facture in a high-pressure die-casting Al-10wt%Si alloy, Mater. Internat. 30 (2020) 221–228.

[6] S.S. Dash, D. Chen, A review on processing-microstructure-property relationships of Al-Si alloys: recent advances in deformation behavior, Metals 13 (2023) 609.

[7] F. Casarotto, A.J. Franke, R. Franke, High-pressure die-cast (HPDC) aluminium alloys for automotive applications, Adv. Mater. Automot. Eng. (2012) 109–149.

[8] S. Cecchel, A. Panvini, G. Cornacchia, Low solution temperature heat treatment of AlSi9Cu3(Fe) high-pressure die-casting actual automotive components, J. Mater. Eng. Perform. 27 (2018) 3791–3802.

[9] J.Y. Hwang, H.W. Doty, M.J. Kaufman, The effects of Mn additions on the microstructure and mechanical properties of Al-Si-Cu casting alloys, Mater. Sci. Eng. A 488 (2008) 496–504.

[10] Y.C. Tsai, C.Y. Chou, S.L. Lee, C.K. Lin, J.C. Lin, S.W. Lim, Effect of trace La addition on the microstructures and mechanical properties of A356 (Al-7Si-0.35Mg) aluminum alloys, J. Alloys Compd. 487 (2009) 157–162.

[11] E.R. Wang, X.D. Hui, S.S. Wang, Y.F. Zhao, G.L. Chen, Improved mechanical properties in cast Al-Si alloys by combined alloying of Fe and Cu, Mater. Sci. Eng. A 527 (2010) 7878–7884.

[12] M. Colombo, E. Gariboldi, A. Morri, Er addition to Al-Si-Mg-based casting alloy: effects on microstructure, room and high temperature mechanical properties, J. Alloys Compd. 708 (2017) 1234–1244.

[13] S. Ji, D. Watson, Z. Fan, M. White, Development of a super ductile diecast Al-Mg-Si alloy, Mater. Sci. Eng. A 556 (2012) 824–833.

[14] D. Kleiven, J. Akola, Precipitate formation in aluminium alloys: multi-scale modelling approach, Acta Mater 195 (2020) 123–131.

[15] K.K. Pius, N.O. Ongwen, M. Mageto, V. Odari, F.M. Gaitho, Mechanical properties of Al-Mg-Si alloys (6xxx series): a DFT-based study, Alloys 2 (2023) 213–226.

[16] A.M.A. Mohamed, F. Samuel, A review on the heat treatment of Al-Si-Cu/Mg casting alloys. Heat treatment: Conventional and novel applications, InTech: Rijeka, Croatia, 2012, pp. 55–72.

[17] J.C. Benedyk, Aluminum Alloys For Lightweight Automotive structures, Mater. Des. Manuf. Light. Veh, Woodhead Publishing Limited, Cambridge, 2010, pp. 79–113.

[18] R. Kobayashi, D. Giofré, T. Junge, M. Ceriotti, W.A. Curtin, Neural network potential for Al-Mg-Si alloys, Phys. Rev. Mater. 1 (2017) 069901.

[19] C. Ravi, C. Wolverton, First-principles study of crystal structure and stability of Al-Mg-Si-(Cu) precipitates, Acta Mater 52 (2004) 4213–4227.

[20] A.K. Gupta, D.J. Lloyd, S.A. Court, Precipitation hardening in Al-Mg-Si alloys with and without excess Si, Mater. Sci. Eng. A 316 (2001) 11–17.

[21] C.D. Marioara, S.J. Andersen, J. Jansen, H.W. Zandbergen, The influence of temperature and storage time at RT on nucleation of the β" phase in a 6082 Al-Mg-Si alloy, Acta Mater 51 (2003) 789–796.

[22] R. Vissers, M.A. van Huis, J. Jansen, H.W. Zandbergen, C.D. Marioara, S. J. Andersen, The crystal structure of the β' phase in Al-Mg-Si alloys, Acta Mater 55 (2007) 3815–3823.

[23] G. Sha, H. Möller, W.E. Stumpf, J.H. Xia, G. Govender, S.P. Ringer, Solute nanostructures and their strengthening effects in Al-7Si-0.6Mg alloy F357, Acta Mater 60 (2012) 692–701.

[24] T. Liu, Z. Pei, D. Barton, G.B. Thompson, L.N. Brewer, Characterization of nanostructures in a high pressure die cast Al-Si-Cu alloy, Acta Mater 224 (2022) 117500.

[25] X.P. Li, G. ji, Z. Chen, A. Addad, Y. Wu, H.W. Wang, J. Vleugels, J. van Humbeeck, J.P. Kruth, Selective laser melting of nano-TiB2 decorated AlSi10Mg alloy with high fracture strength and ductility, Acta Mater 129 (2017) 183–193.

[26] Y. Xu, Y. Zhang, J. Li, P. Wang, J. Wang, H. Chen, H. Sun, H. Zhan, Effects of Cr-addition on ageing response of an Al-Si-Mg die cast alloy, Mater. Sci. Eng. A 892 (2024) 146058.

[27] A.C.P. Jain, D. Marchand, A. Glensk, M. Ceriotti, W.A. Curtin, Machine learning for metallurgy III: a neural network potential for Al-Mg-Si, Phys. Rev. Mater. 5 (2021) 053805.

[28] C. Pareige, M. Roussel, S. Novy, V. Kuksenko, P. Olsson, C. Domain, P. Pareige, Kinetic study of phase transformation in a highly concentrated Fe-Cr alloy: monte Carlo simulation *versus* experiments, Acta Mater 59 (2011) 2404–2411.

[29] H. Miyoshi, H. Kimizuka, A. Ishii, S. Ogata, Temperature-dependent nucleation kinetics of Guinier-Preston zones in Al-Cu alloys: an atomistic kinetic Monte Carlo and classical nucleation theory approach, Acta Mater 179 (2019) 262–272.

[30] Y. Feng, M. Liu, Y. Shi, H. Ma, D. Li, Y. Li, L. Lu, X. Chen, High-throughput modeling of atomic diffusion migration energy barrier of fcc metals, Prog. Nat. Sci. 29 (2019) 341–348.

[31] M. Mantina, Y. Wang, R. Arroyave, L. Chen, Z. Liu, C. Wolverton, First-principles calculation of self-diffusion coefficients, Phys. Rev. Lett. 100 (2008) 215901.

[32] Z. Xi, L.G. Hector Jr, A. Misra, L. Qi, Kinetic Monte Carlo simulations of solute clustering during quenching and aging of Al-Mg-Zn alloys, Acta Mater 269 (2024) 119795.

[33] M. Athenes, P. Bellon, G. Martin, Identification of novel diffusion cycles in b2 ordered phases by monte carlo simulation, Philos. Mag. A 76 (1997) 565–585.

[34] M. Athenes, P. Bellon, G. Martin, Effects of atomic mobilities on phase separation kinetics: a monte-carlo study, Acta Mater 48 (2000) 2675–2688.

[35] D.R. Mason, R.E. Rudd, A.P. Sutton, Stochastic kinetic monte carlo algorithms for long-range hamiltonians, Comput. Phys. Commun. 160 (2004) 140–157.

[36] Q. Ye, J. Wu, J. Zhao, G. Yang, B. Yang, Kinetic Monte Carlo simulation of clustering in an Al-Mg-Si-Cu Alloy, Materials 14 (2021) 4523.

[37] Z. Xi, M. Zhang, L.G. Hector Jr., A. Misra, L. Qi, Mechanism of local lattice distortion effects on vacancy migration barriers in fcc alloys, Phys. Rev. Mater. 6 (2022) 073601.

[38] B. Xu, J. Zhang, S. Ma, Y. Xiong, S. Huang, J.J. Kai, S. Zhao, Revealing the crucial role of rough energy landscape on self-diffusion in high-entropy alloys based on machine learning an kinetic Monte Carlo, Acta Mater 234 (2022) 118051.

[39] H. Liao, H. Kimizuka, A. Ishii, J.P. Du, S. Ogata, Nucleation kinetics of the β″ precipitate in dilute Mg-Y alloys: a kinetic Monte Carlo study, Scr. Mater. 210 (2022) 114480.

[40] S. Batzner, A. Musaelian, L. Sun, M. Geiger, J.P. Mailoa, M. Kornbluth, N. Molinari, T.E. Smidt, B. Kozinsky, E(3)-equivariant graph neural networks for data-efficient and accurate interatomic potentials, Nat. Commun. 13 (2022) 2453.

[41] A. Musaelian, S. Batzner, A. Johansson, L. Sun, C.J. Owen, M. Kornbluth, B. Kozinsky, Learning local equivariant representations for large-scale atomistic dynamics, Nat. Commun. 14 (2023) 579.

[42] C. Liu, Y. Wang, Y. Wang, M. Islam, J. Hwang, Y. Wang, Y. Fan, Concurrent prediction of metallic glasses' global energy and internal structural heterogeneity by interpretable machine learning, Acta. Mater 259 (2023) 119281.